Interaction potentials for alumina and molecular dynamics simulations of amorphous and liquid alumina

Priya Vashishta,[a] Rajiv K. Kalia,[1] Aiichiro Nakano,[1] and José Pedro Rino[1,2]
[1]*Collaboratory for Advanced Computing and Simulations, Department of Chemical Engineering and Materials Science, Department of Physics and Astronomy, and Department of Computer Science, University of Southern California, Los Angeles, California 90089-0242, USA*
[2]*Departamento de Física, Universidade Federal de São Carlos, São Carlos SP 13565-905, Brazil*

(Received 16 September 2007; accepted 28 January 2008; published online 16 April 2008)

Structural and dynamical properties of crystalline alumina α-Al_2O_3 and amorphous and molten alumina are investigated with molecular dynamics simulation based on an effective interatomic potentials consisting of two- and three-body terms. Structural correlations are examined through pair distribution functions, coordination numbers, static structure factors, bond angle distributions, and shortest-path ring analyses. The calculated results for neutron and x-ray static structure factors are in good agreement with experimental results. Dynamical correlations, such as velocity autocorrelation function, vibrational density of states, current-current correlation function, and frequency-dependent conductivity, are also discussed. © *2008 American Institute of Physics*. [DOI: 10.1063/1.2901171]

I. INTRODUCTION

Aluminum oxide (alumina, Al_2O_3) is a highly insulating ceramic with great technological applications. It is as important as silica due to its basic uses for preventing crystallization and giving chemical stability and durability to a glaze, for instance. Due to its high melting point, very high hardness, and low electrical conductivity, it is used in cutting tools, electronic devices, optics, and catalyst support, among others.[1] Besides its technological applications, alumina as well as Mg, Ca, and Si oxides are part of Earth's mantle and an understanding of their properties in extreme condition of temperature and pressure is very important for a systematic understanding of Earth's mantle.[2,3] Alumina, aside from its most stable corundum α-Al_2O_3 form, exists in several metastable polymorphs, β, δ, γ, η, θ, κ, and χ phases. These polymorphs are divided into two categories according to the structural arrangement of the oxygen atoms: structures with fcc oxygen symmetries include γ, η (cubic), θ (monoclinic), and δ (tetragonal or orthorhombic) phases, whereas structures with oxygen based on hcp packing are represented by α (trigonal), κ (orthorhombic), and χ (hexagonal) phases. Other monoclinic phases, θ', θ'', and λ, have also been identified.[4] A review of these crystal structures and their precursors can be found in the work of Levin and Brandon.[4]

Amorphous alumina formed by rapid solidification has been reported on chill surface of plasma sprayed deposits,[5] by using vapor deposition,[6] reactive sputtering,[7] evaporative decomposition of solution,[8] and electrohydrodynamic atomization.[9] Structural determination of poor quality amorphous alumina samples obtained by anodic oxidation of aluminum foil has also been reported.[10]

Liquid alumina, on the other hand, is less studied than its solid phases, mainly due to experimental difficulty. At very high temperatures, the structural information is influenced by the container contamination. These problems can be eliminated by using levitation techniques, in which a laser melts the sample. Several experiments have been done by using the levitation technique in liquid alumina. Ansell *et al.*[11] and Waseda *et al.*[12] performed an x-ray experiment, Landron *et al.*,[13,14] performed neutron scattering measurements, and Florian *et al.*[15] and Coutures *et al.*[16] have carried out nuclear magnetic resonance measurements. More recently, Krishnan *et al.* have carried out new structural measurements of liquid alumina over a wide range of temperature by using x-ray diffraction and different atmospheres in a levitating specimen.[17]

A fundamental challenge for theoretical and simulation study of alumina is to find an interatomic interaction potential for satisfactory description of crystalline, amorphous, and liquid states of alumina. The theoretical studies of some crystalline phases have been reported. For example, Guo *et al.* reported a first-principles electronic structure calculation on sapphire and its surfaces.[18,19] Boettger calculated the total energy of the corundum phase with all-electron, full-potential linear combinations of Gaussian-type orbital-fitting function technique, which shows good agreement with experiments.[20] Holm *et al.* calculated elastic and optical properties of α- and κ-alumina by using plane-wave and full-potential linearized muffin tin orbital methods.[21] The structure of κ-Al_2O_3 has been calculated by Yourdshanhyan *et al.* by using first-principles methods.[22,23] The κ-Al_2O_3 has also been described through several interatomic potentials, all of them based on the Born ionic model, see for instance the works of Bush *et al.*,[24] Catlow *et al.*,[25] Minervini *et al.*,[26] Mackrodt and Stewart,[27] and Paglia *et al.*[28] The structure and energetics of basal-plane surface of α-alumina were calculated by Manassidis *et al.* by using fully self-consistent *ab initio* calculations.[29] By using density functional theory with plane-wave basis and pseudopotentials, Gutierrez *et al.* explained the structure of γ-alumina in terms of a defected spinel structure with cation site vacancies randomly distrib-

[a]Electronic mail: priyav@usc.edu.

uted between octahedral and tetrahedral positions, which is consistent with crystallographic data,[30] and Menéndez-Proupin and Gutiérrez[31] report the electronic properties of bulk γ-phase. Alvarez *et al.* performed molecular dynamics (MD) simulations by using a Pauling-type interaction potential to study the structure and micropore formation mechanisms in γ-Al_2O_3.[32,33] Blonski and Garofalini performed MD simulations by using the Born–Mayer–Huggins potential together with a three-body interaction in α- and γ-alumina both in bulk and at surfaces.[34] The structure of γ-alumina was also determined by using an interatomic potential and first-principles calculation by Paglia *et al.*[35] Gutiérrez *et al.* studied the mechanism for κ- to α-Al_2O_3 transition by using MD simulation with a pairwise interatomic potential.[36] Recently, Jahn *et al.* proposed a flexible ionic interaction model for alumina, where the parameters are optimized by reference to *ab initio* density functional theory electronic structure calculations.[37] The structural properties of amorphous alumina have been reported by MD simulation by using the Matsui[38] potential.[30]

Considerably, less research effort has been devoted to the structural description of liquid alumina. Ahuja *et al.* determined the melting and the liquid structure by means of a two-phase MD method with a pair potential.[39] Gutierrez *et al.*[36] and San Miguel *et al.*[40] studied the structural properties of liquid alumina by using MD simulation with a pair potential. Krishnan *et al.*[17] performed MD simulation with an interaction potential that was proposed by Jahn *et al.*[37]

In this paper, we present an effective interatomic interaction potential for α-Al_2O_3, amorphous, and liquid alumina. Structural properties are studied through pair correlation functions, coordination numbers, bond angle distributions, ring analysis, and x-ray and neutron static structure factors. Dynamical properties such as vibrational density of states and electric current-current functions are also calculated. The paper is divided into seven sections. In Sec. II, the proposed interaction potential is described. Section III is dedicated to the analysis of the structure of the amorphous alumina. In Sec. IV, we discuss structural correlations in the liquid phase. The analysis of rings structures is presented in Sec. V, and the vibrational density of states and the electrical current-current correlations for amorphous and liquid Al_2O_3 are analyzed in Sec. VI. Finally, conclusions are presented in Sec. VII.

II. INTERATOMIC INTERACTION POTENTIAL FOR Al_2O_3

The proposed interatomic potential consists of two- and three-body interactions. The potential energy of the system can be written as

$$V = \sum_{i<j} V_{ij}^{(2)}(r_{ij}) + \sum_{i,j<k} V_{jik}^{(3)}(r_{ij}, r_{ik}). \tag{1}$$

This interaction potential has the functional form used to describe other materials.[41–45] The two-body term includes steric-size effects, Coulomb interactions, charge-induced dipole, and van der Waals interactions. The two-body part of the potential is given by

$$V_{ij}^{(2)}(r) = \frac{H_{ij}}{r^{\eta_{ij}}} + \frac{Z_i Z_j}{r} e^{-r/\lambda} - \frac{D_{ij}}{r^4} e^{-r/\xi} - \frac{W_{ij}}{r^6}. \tag{2}$$

In Eq. (2), H_{ij} is the strength of the steric repulsion, Z_i is the effective charge in units of the electronic charge $|e|$, D_{ij} and W_{ij} are the strengths of the charge-dipole and van der Waals attractions, respectively, η_{ij} are the exponents of the steric repulsion, and λ and ξ are the screening lengths for the Coulomb and charge-dipole interactions, respectively. Here, $r \equiv r_{ij} = |\mathbf{r}_i - \mathbf{r}_j|$ is the distance between the ith atom at position $\mathbf{r}_i$ and the jth atom at position $\mathbf{r}_j$.

The two-body interatomic potential is truncated at $r_{cut} = 6.0$ Å and is shifted for $r \leq r_{cut}$ to have the potential and its first derivative continuous at r_{cut}.[46,47] The shifted two-body part of the interatomic potential is given by

$$V_{ij}^{(2\ \text{shifted})}(r) = \begin{cases} V_{ij}^{(2)}(r) - V_{ij}^{(2)}(r_c) - (r - r_c)[dV_{ij}^{(2)}(r)/dr]_{r=r_c}, & r \leq r_c \\ 0, & r > r_c, \end{cases} \tag{3}$$

The screening in the Coulomb and charge-dipole interactions is included to avoid the long range nature of the bare interactions. The main advantage of the short range nature of the interactions is its computational efficiency, which increases by an order of magnitude when compared to the bare interactions. It has been shown that the inclusion of the screening has no noticeable difference in the structural and dynamical properties whether the potential is screened or not.[47]

The three-body interaction potential is given by a product of spatial and angular dependent factors to correctly describe bond-bending and bond-stretching characteristics, which has been discussed in detail elsewhere,[48]

$$V_{jik}^{(3)}(r_{ij}, r_{ik}) = R^{(3)}(r_{ij}, r_{ik}) P^{(3)}(\theta_{jik}), \tag{4}$$

where

$$R^{(3)}(r_{ij}, r_{ik}) = B_{jik} \exp\left(\frac{\gamma}{r_{ij} - r_0} + \frac{\gamma}{r_{ik} - r_0}\right) \Theta(r_0 - r_{ij}) \Theta(r_0 - r_{ik}), \tag{5}$$

TABLE I. Comparison of cohesive energy E/N, bulk modulus B and elastic constants $C_{\alpha\beta}$ for α-Al_2O_3 between MD model and experiments. The experimental data for the elastic constants are from Ref. 49.

	MD	Expt.
E/N (eV/at.)	−6.35	−6.35
B (GPa)	253	255
C_{11} (GPa)	523	498
C_{12} (GPa)	147	163
C_{13} (GPa)	129	117
C_{14} (GPa)	7.5	−23
C_{33} (GPa)	427	502
C_{44} (GPa)	135	147
C_{66} (GPa)	174	167[a]

[a]Calculated from the relation $C_{66}=(C_{11}-C_{12})/2$.

$$P^{(3)}(\theta_{jik}) = \frac{(\cos\theta_{jik} - \cos\bar{\theta}_{jik})^2}{1 + C_{jik}(\cos\theta_{jik} - \cos\bar{\theta}_{jik})^2}, \quad (6)$$

where B_{jik} is the strength of the three-body interaction, θ_{jik} is the angle formed by $\mathbf{r}_{ij}$ and $\mathbf{r}_{ik}$, $\bar{\theta}_{jik}$ and C_{jik} are constants, and $\Theta(r_0-r_{ij})$ is the step function.

The three-body interactions are only applied to the triplets of atoms that are connected by the Al–O cohesive bonds. Out of the six possible three-body combinations, there are only two combinations, Al–O–Al and O–Al–O, which have the Al–O cohesive bond. Owing to the partially ionic nature of the A–O bond that gives positive charge to Al to form Al^{3+} and negative charge to O to form O^{2-}, there is no cohesive bond between Al–Al and O–O.

Following previous studies by using the same form of interatomic potential, the exponents η_{ij} were chosen to be 7, 9, and 7 for Al–Al, Al–O, and O–O interactions, respectively. The screening lengths are $\lambda=5.0$ Å and $\xi=3.75$ Å. The other parameters in the interaction potential are determined by using the experimental values for lattice constant, cohesive energy, bulk modulus, and some elastic constants for α-Al_2O_3. Table I compares the experimental and calculated quantities using our interaction potential, and Table II lists the parameters for Al_2O_3 interatomic potential.

The primary goal of the proposed interaction potential for alumina is to describe structural properties and dynamical behavior of α-Al_2O_3, molten, and amorphous alumina and their interfaces with metals and ceramics. It is unlikely that an interaction with simple three-body interactions, as proposed here, can accurately describe the subtle differences in various crystalline phases of alumina.

All MD simulations reported in this paper were performed for a system with 8640 atoms (3456 Al+5184 O) for several densities. Periodic boundary conditions were imposed, and Newton's equations of motion were integrated using the velocity Verlet algorithm with a time step of 1.5×10^{-15} s.

III. ELASTIC PROPERTIES AND MELTING OF A-Al_2O_3

The interaction potential has been further validated by calculating the density dependence of elastic constants and the melting temperature. Figure 1 shows the total energy per particle as a function of the volume per particle of α-Al_2O_3. The dashed line is a Murnaghan equation of state[50] fit resulting in a bulk modulus of 249 GPa, cohesive energy of −6.35 eV/at., and the first derivative of the bulk modulus, $B'=6.4$. The interaction potential describes the system with minimum energy at experimental density.

TABLE II. Parameters for two- and three-body parts of the interaction potential used in the MD simulation of structural and dynamical properties of amorphous and liquid Al_2O_3.

	Al	O	
Z_i (e)	1.5237	−1.0158	
$\lambda=5.0$ Å	$\xi=3.75$ Å	$r_c=6.0$ Å	$e=1.602\times10^{-19}C$

Two body

	Al–Al	Al–O	O–O
η_{ij}	7	9	7
H_{ij} (eV Å$^{\eta}$)	12.7506	249.3108	564.7334
D_{ij} (eV Å^4)	0	50.1522	44.5797
W_{ij} (eV Å^6)	0	0	79.2884

Three body

	B_{jik} (eV)	$\bar{\theta}_{jik}$ (deg)	C_{jik}	γ (Å)	r_0 (Å)
Al–O–Al	8.1149	109.47	10	1.0	2.90
O–Al–O	12.4844	90.0	10	1.0	2.90

A. Elastic properties of alumina

The calculated elastic constants of α-alumina, as a function of density, are shown in Fig. 2. The simulation shows that C_{14} is unaffected by the change of density, while all other elastic constants decrease with decreasing density.

B. The melting of alumina

The melting temperature of alumina has been determined in two ways. In one procedure, a system containing 8640 atoms with periodic boundary conditions in all directions is simulated in the constant-temperature-and-pressure

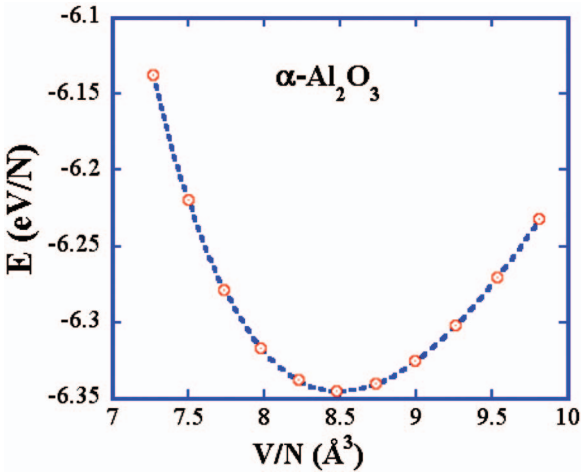

FIG. 1. (Color) Energy per particle as a function of volume per particle. The dashed line is a Murnaghan equation of state fit. $(E(V)=[BV/B'(B'-1)]\times[B'(1-V_0/V)+(V_0/V)^{B'}-1]+E(V_0))$ (Ref. 50).

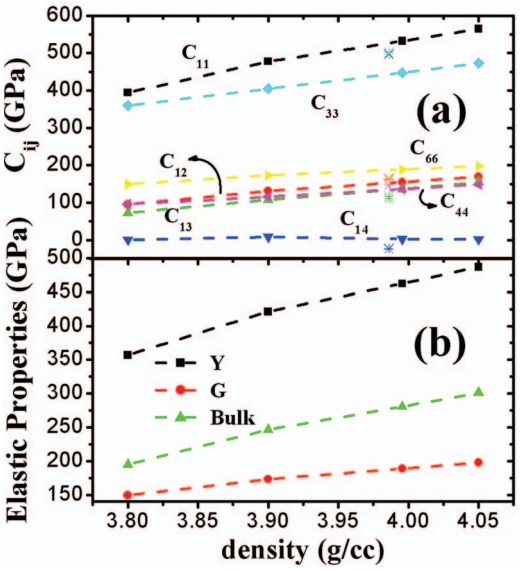

FIG. 2. (Color) (a) Elastic constants and (b) elastic moduli (Young's modulus Y, shear modulus G, and bulk modulus B) for α-Al_2O_3 as a function of density.

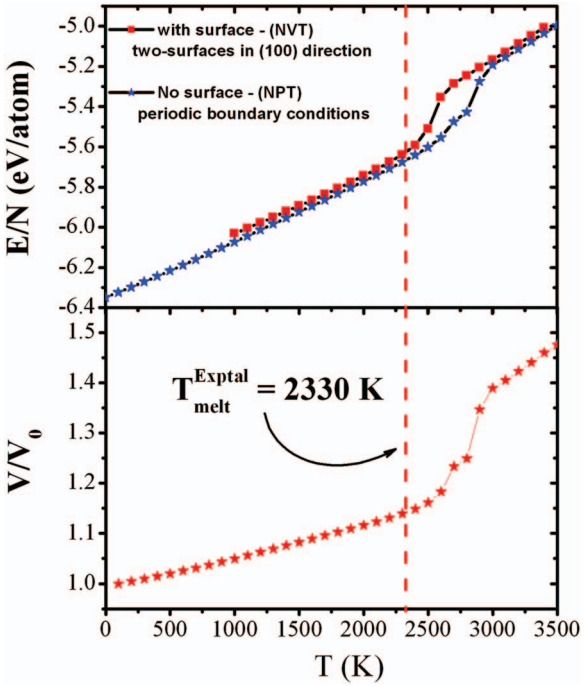

FIG. 3. (Color) Melting of Al_2O_3. MD energy per atom (top) and fractional volume (bottom) as a function of temperature. The vertical dashed line is the experimental reported melting temperature.

(*NPT*) ensemble. The temperature is increased in steps of 100 K until 3500 K. At each temperature, the system is run for 10 000 Δt, and averages are taken over additional 10 000 time steps. The calculated melting temperature is found to be around 2700 K, whereas the experimental value is 2330 K.

In the second procedure, two free surfaces are created in the z direction [direction (0001)]. A constant-temperature simulation is performed, following the same heating procedure as in the first procedure. It should be noted that MD melting is studied for a defect-free crystal under ideal conditions. One must always expect the melting temperature to be a few percent higher than the experimental values where the sample always has defects and conditions are less than ideal, e.g., container effects and oxygen loss causing loss of stoichiometry. In this case, as expected, the MD melting temperature is lowered to ~2500 K due to the free surfaces. In Fig. 3, the energy per atom and the fractional MD volume are shown as a function of temperature, where the dashed vertical line marks the experimental melting temperature for alumina.[13,39] The calculated change in volume at melting is about of 20%, which is consistent with the reported volume change on freezing.[51]

IV. ELASTIC PROPERTIES OF AMORPHOUS ALUMINA (A-Al_2O_3)

Amorphous systems have been prepared by cooling molten alumina at several different densities, and the linear elastic constants have been calculated at zero temperature. Figure 4 shows all three elastic constants and the elastic moduli as a function of density for amorphous alumina. All the elastic constants decrease for lower densities, with the shear modulus showing the smallest dependence on density. Poisson ratio is determined to be ν=0.22, which agrees well with an experimentally reported value of 0.231 for sintered ceramic.[52]

V. STRUCTURAL CORRELATIONS IN REAL AND RECIPROCAL SPACES

In this section, the structural correlations in the liquid and amorphous states are discussed both in real (r) and reciprocal (q) spaces. In the real space, the two-body structural correlations are analyzed through pair distribution functions, and in the reciprocal space through their Fourier transform, the static structure factor. The partial pair distribution functions are calculated from

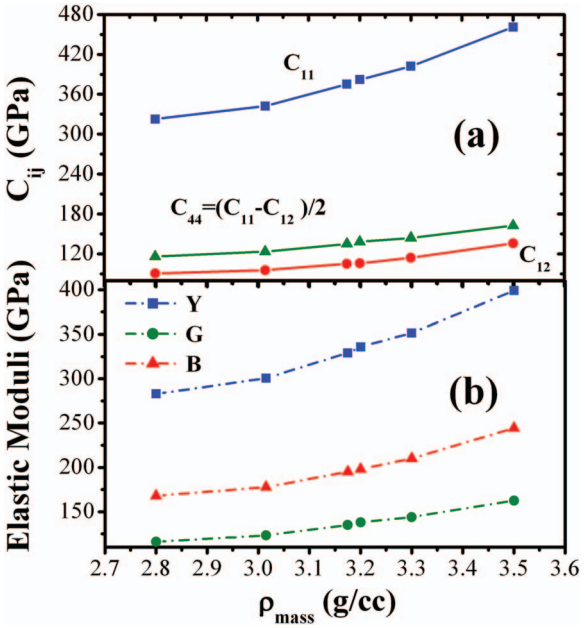

FIG. 4. (Color) (a) Elastic constants and (b) elastic moduli (Youngs, Y, shear, G, and bulk, B, moduli) for amorphous alumina at zero temperature as a function of density.

$$\langle n_{\alpha\beta}(r)\rangle \Delta r = 4\pi r^2 \rho c_\beta \Delta r g_{\alpha\beta}(r) \quad (\alpha,\beta = \text{Al or O}), \tag{7}$$

where ρ is the total number density, $\langle n_{\alpha\beta}(r)\rangle \Delta r$ is the number of β particles in a shell between r and $r+\Delta r$ around an α particle, c_β is the concentration of β particles, and the brackets denotes an ensemble average as well the averaging over all α particles. The coordination number $C_{\alpha\beta}(r)$, which determines the average number of β particles around an α particle, is an integral of the corresponding partial pair distribution function,

$$C_{\alpha\beta}(R) = 4\pi\rho c_\beta \int_0^R r^2 g_{\alpha\beta}(r) dr. \tag{8}$$

The total pair, neutron, and charge-charge distribution functions are, respectively, defined as[42]

$$g(r) = \sum_{\alpha,\beta} c_\alpha c_\beta g_{\alpha\beta}(r), \tag{9}$$

$$g_n(r) = \frac{\Sigma_{\alpha,\beta} c_\alpha b_\alpha c_\beta b_\beta g_{\alpha\beta}(r)}{(\Sigma_\alpha c_\alpha b_\alpha)^2}, \tag{10}$$

$$g_{ZZ}(r) = \frac{\Sigma_{\alpha,\beta} c_\alpha Z_\alpha c_\beta Z_\beta g_{\alpha\beta}(r)}{\Sigma_\alpha c_\alpha Z_\alpha^2}, \tag{11}$$

where b_α is the coherent neutron scattering cross section and Z_α is the effective charge for α-type ion.

The properties of the system in the q space are analyzed through the static structure factors. The partial static structure factors are obtained by performing the Fourier transformation of the corresponding pair distribution functions, i.e.,

$$S_{\alpha\beta}(q) = \delta_{\alpha\beta} + 4\pi\rho(c_\alpha c_\beta)^{1/2} \int_0^\infty [g_{\alpha\beta}(r) - 1] \frac{r^2 \sin(qr)}{qr} dr. \tag{12}$$

From these partial static structure factors, we can compute the neutron, x-ray, and charge-charge static structure factors as

$$S_n(q) = \frac{\Sigma_{\alpha,\beta} b_\alpha b_\beta (c_\alpha c_\beta)^{1/2} S_{\alpha\beta}(q)}{(\Sigma_\alpha b_\alpha^2 c_\alpha)}, \tag{13}$$

$$S_X(q) = \frac{\Sigma_{\alpha,\beta} f_\alpha f_\beta (c_\alpha c_\beta)^{1/2} S_{\alpha\beta}(q)}{(\Sigma_\alpha f_\alpha^2 c_\alpha)}, \tag{14}$$

$$S_{zz}(q) = \frac{\Sigma_{\alpha,\beta} Z_\alpha Z_\beta (c_\alpha c_\beta)^{1/2} S_{\alpha\beta}(q)}{\Sigma_\alpha Z_\alpha^2 c_\alpha}. \tag{15}$$

where f_α are the x-ray form factors taken from Ref. 14.

A. Structural correlations for amorphous Al_2O_3 in real space

Once we have established the validity of the interatomic potential through cohesive energy, elastic constants, bulk modulus, and melting temperature of the corundum Al_2O_3, several simulations with the same interaction potential have been performed to describe the structural and dynamical properties of amorphous and liquid alumina.

Amorphous alumina (a-Al_2O_3) has been prepared by cooling the melt. Starting from a crystalline α-Al_2O_3, the system is gradually heated until a very well thermalized, high temperature liquid at 3000 K is obtained. From this liquid, the system is cooled to 300 K, and it is thermalized for 50 000 time steps ($\Delta t = 1.8$ fs). Averages are taken over additional 10 000 time steps. This procedure is performed for three densities: 2.81 and 3.175 g/cc (experimentally reported densities)[13,51] as well as 3.30 g/cc.

Figure 5 shows the total pair distribution function and each partial correlation at 300 K for densities $\rho = 2.81$ and 3.175 g/cc. For the larger density, there is only a small difference in coordination number. All the features in the correlation functions are practically the same. The first peak in $g_{\text{Al–O}}$ correlation occurs at 1.85 ± 0.05 Å, which corresponds to the Al–O bond length. The coordination number up to 2.27 Å is found to be 4.44. The second peak at 2.72 Å in $g(r)$ is mainly due to O–O correlations. Aluminum-aluminum correlations display a shoulder at 2.71 Å, and the main first peak at 3.11 Å. Table III compares the peak position and the full width at half maximum (FWHM) for the first peak in each partial correlation for the two densities studied. Even for an amorphous system that is 4% denser ($\rho = 3.30$ g/cc), the peak positions and its width are essentially the same.

It is interesting to note that in octahedrally coordinated α-Al_2O_3 at 300 K, the Al–O bond distances are 1.852 and 1.971 Å, with the average value of 1.91 Å,[53] whereas in polymorphs that have some tetragonal character such as η-, γ-, and θ-alumina, these bond distances range from 1.641 to 1.94 Å, with an average value of 1.813 Å for η-alumina, from 1.777 to 2.244 Å, with average of 1.937 Å for γ-alumina, and from 1.710 to 2.025 Å, with average of 1.866 Å for θ-alumina. The average Al–O bond length of the octahedral η-, γ-, and θ-alumina varies from 1.94 to 1.95 Å, which is much larger than that of α-Al_2O_3.[54]

The knowledge of atomic positions allows the determination of the bond angle distributions for amorphous phase. Figure 6 shows this distribution for the amorphous phase at 300 K and 2.81 g/cc.

It is interesting to observe that the distribution of O–Al–O bond angles in amorphous phase resembles the equivalent angle distribution of the polymorph θ phase, as shown in Table IV. This could be an indication that the amorphous phase transforms to a crystal θ phase before recrystallizing in the most stable corundum α-Al_2O_3. The peak positions of these bond angle distributions are, in general, very similar to those reported by Gutiérrez and Johansson.[55]

B. Structural correlations for amorphous Al_2O_3 in reciprocal space

From the MD trajectories, the suitably weighted neutron and x-ray static structure factors have been calculated. In Fig. 7, we depict the partial and total structure factors for simulated amorphous alumina at 300 K and 2.81 g/cc. The density-density correlation for amorphous system displays a shoulder at around 1.90 $Å^{-1}$ and other peaks at 2.81, 4.40, 7.38, and 10.65 $Å^{-1}$. The shoulder arises from the Al–O an-

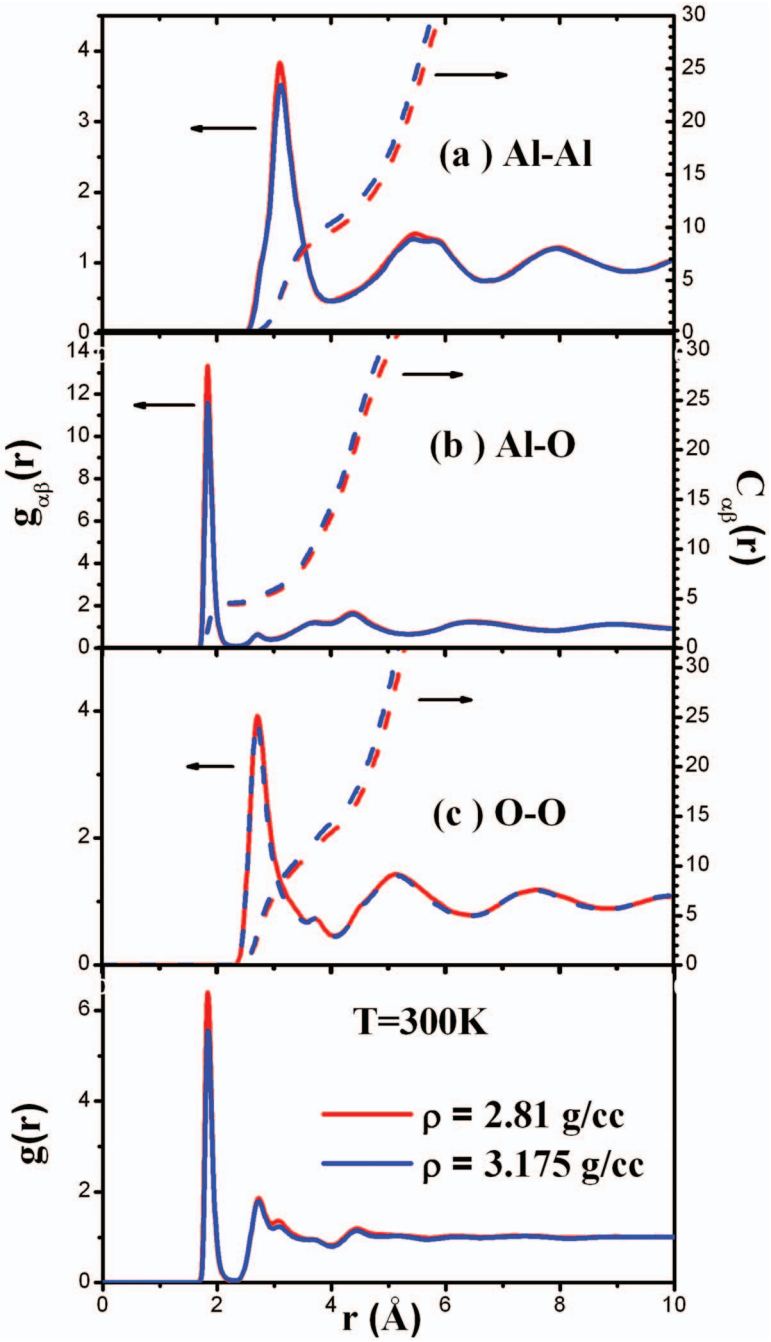

FIG. 5. (Color) MD results for partial and total pair distribution functions for amorphous alumina at 300 K and two densities.

ticorrelations. The main peak at 2.81 is due to all three (Al–Al, Al–O, and O–O) correlations. The minimum at around 6 $Å^{-1}$ is due to the cancellation of Al–Al and O–O correlations [see Fig. 7(b)].

TABLE III. Position and full width at half maximum of the first peak in partial pair distribution functions from molecular dynamics simulations for amorphous alumina at 300 K and at two densities.

Density (g/cc)	Distance	Position (Å)	FWHM (Å)
2.81	Al–Al	3.11	0.68
	Al–O	1.84	0.12
	O–O	2.73	0.41
3.300	Al–Al	3.12	0.65
	Al–O	1.85	0.16
	O–O	2.70	0.42

Calculated neutron and x-ray static structure factors for amorphous alumina at 2.81 g/cc and 300 K are depicted in Fig. 8. Once each scattering is weighted with different factors (coherent neutron cross section or x-ray form factor), the region of small q displays slightly different peak positions.

C. Structural correlations in liquid Al_2O_3

The liquid state has been obtained after heating a corundum α-Al_2O_3 structure up to 3500 K. After allowing the system to be thermalized for 50 000 time steps, three liquid systems at 2600 K are prepared at three densities: two experimentally reported values [2.81 g/cc (Refs. 13 and 56) and 3.175 g/cc (Refs. 11 and 51)] as well as a denser one at 3.30 g/cc. At this temperature, structural correlations are calculated by taking averages over 10 000 time steps.

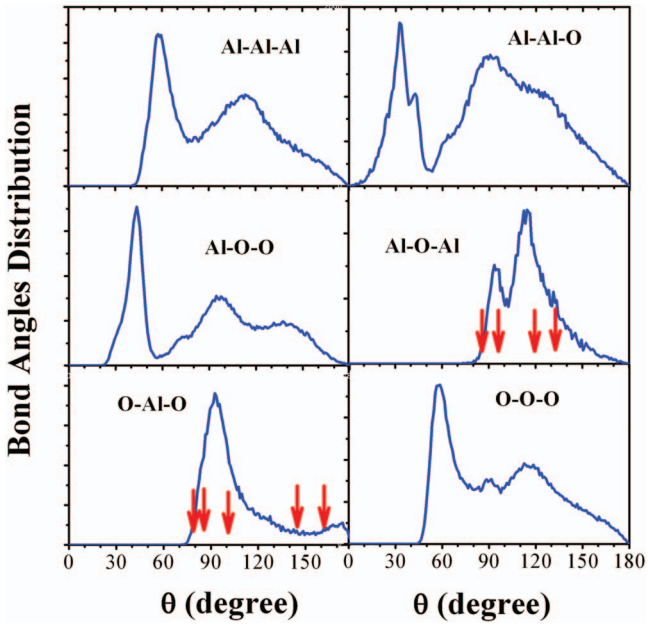

FIG. 6. (Color) Bond angle distribution for amorphous alumina at 300 K and 2.81 g/cc from MD simulations. The arrows show the angles for the α-Al_2O_3 crystal (see Ref. 53).

1. Structural correlations in real space

The two-body correlation for liquid alumina at 2600 K is analyzed by using partial and total pair distribution functions as well as coordination numbers. Several MD simulations have been performed for liquid alumina.[36,40,57] However, in all of them, the densities were higher than the experimental value. Figure 9 compares the total neutron pair distribution function derived from experimental data[14,13] and that calculated from MD. The neutron weighted distribution function $g_N(r)$ shows a sharp peak at 1.76 ± 0.01 Å and a second peak at around 2.8 Å. From the partial pair distribution functions in Fig. 10, the first peak, which defines the bond length of Al–O, is found to be 1.78 ± 0.05 Å, with the coordination number, 4.41, calculated up to 2.45 Å in excellent agreement with experimentally reported values. It is important to note that, for a higher density, the coordination number is slightly

TABLE IV. Distribution of angles in selected crystalline phases and in simulated amorphous phase.

	O–Al–O (deg) bond angles and its multiplicity (in parenthesis)
α-Al_2O_3 (corundum)[a]	79.53, 86.40, 101.20, 164.13
η-Al_2O_3[b]	87.69 (6), 92.31 (6), 95.68 (1), 108.14 (4), 119.09 (3), 124.72 (1), 180.0 (3)
γ-Al_2O_3[b]	80.57 (3), 87.78 (6), 86.0 (6), 92.22 (6), 104.53 (3), 109.47 (6), 119.09 (3), 162.34 (3), 180.0 (6)
θ-Al_2O_3[b]	82.63 (2), 84.26 (2), 91.65 (1), 92.09 (2), 92.27 (2), 92.64 (2), 99.43 (1), 106.51 (2), 106.66 (2), 114.54 (1), 116.25 (1), 172.39 (1), 173.85 (2)
Amorphous	93, 171

[a]Reference 53.
[b]Reference 54.

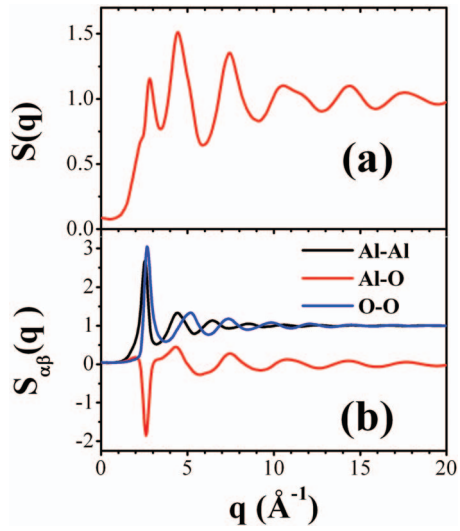

FIG. 7. (Color) Calculated (a) density-density structure factor and (b) partial structure factors for amorphous alumina at 300 K and 2.81 g/cc.

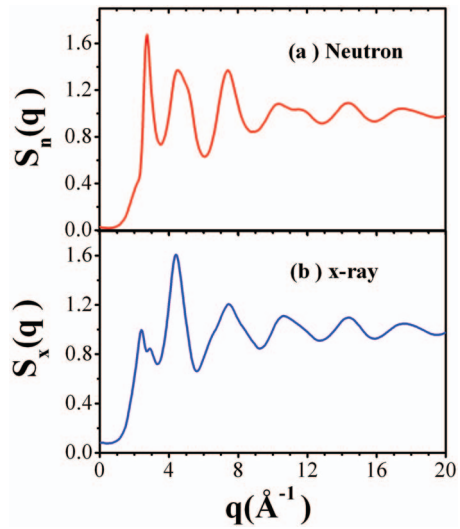

FIG. 8. (Color) The calculated (a) neutron and (b) x-ray static structure factors for amorphous alumina at 2.81 g/cc and 300 K.

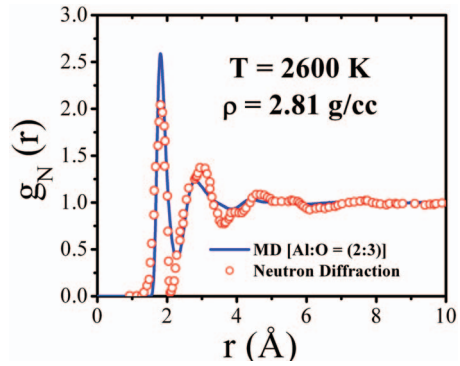

FIG. 9. (Color) Total neutron pair distribution function for liquid Al_2O_3 at 2600 K and 2.81 g/cc derived from experimental data and from MD calculations.

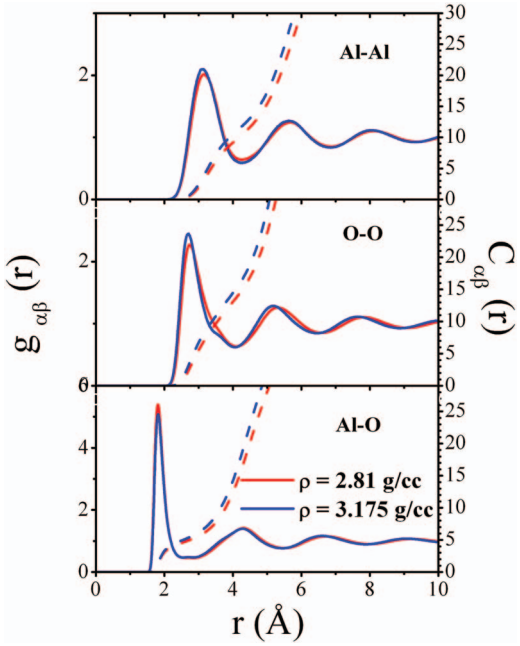

FIG. 10. (Color) Molecular dynamics partial pair distribution function and coordination numbers calculated at 2600 K and 2.81 and 3.175 g/cc.

larger, although the peak positions are the same. The coordination number for ρ=3.175 g/cc is 4.78, using the same cutoff length.

The three-body correlation is described through bond angle distributions. Figure 11 shows the six bond angles for liquid alumina at 2600 K and 2.81 g/cc. The O–Al–O bond angle has a peak at 90°, with a large dispersion. This angle, together with the coordination number of ~4, characterizes the liquid state as being built from disordered tetrahedral units, in contrast to the octahedrally coordinated crystalline structures. These tetrahedral units are linked to produce a network with Al–O–Al peaked at 109°. The arrows in the O–Al-O bond angle distribution are the angles in the corundum phase. The network of tetrahedral units will be discussed later in terms of ring statistics.

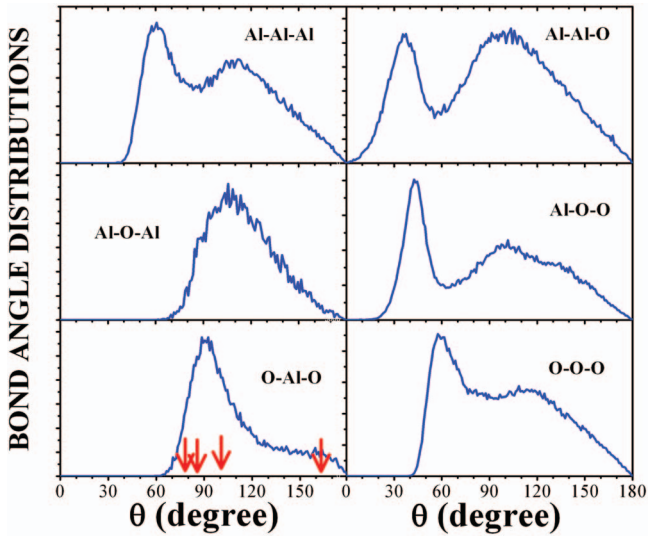

FIG. 11. (Color) Calculated bond angles distributions for liquid alumina at 2600 K and 2.81 g/cc.

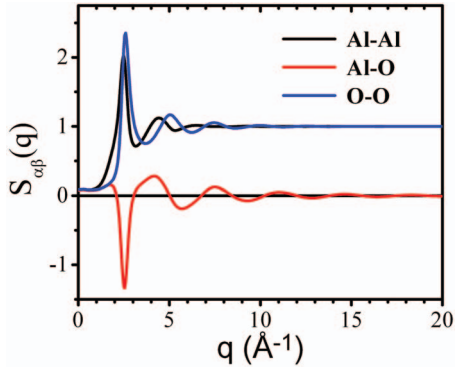

FIG. 12. (Color) Calculated static structure factor for molten alumina at 2600 K and 2.81 g/cc.

2. Structural correlations in reciprocal space

Figure 12 shows the calculated partial static structure factors, and in Figs. 13 and 14, we compare the calculated neutron and x-ray static structure factors with corresponding experimental results. In Figs. 13 and 14, the neutron and X-ray static structure factors are calculated, using the ratio of 2:3 for the concentrations of Al and O.

The x-ray experiment on levitated molten alumina is carried out at high temperatures. This leads to a loss of oxygen from the sample resulting in nonstoichiometry and oxygen deficient sample. To study the effect of oxygen deficiency on the static structure factors, neutron and x-ray structure factors have been calculated with the concentration ratio of 1:1. Figure 15 shows the calculated neutron static structure factor with oxygen deficiency. Note that the height of the first peak decreases, when there is less oxygen atoms. In Fig. 16, the calculated x-ray static structure factor considering oxygen deficiency is shown, along with experimental data.

Although Ansell *et al.* used a density of 3.175 g/cc in their analyses, and the directed measured density was 2.81 g/cc,[56] the difference of 13% in the density in the calculated structure factors is reflected only below 2 Å^{-1}. Both neutron and x-ray scattering structure factors in experiments are well reproduced by the MD simulation. In neutron diffraction experiments, a shoulder at 1.81 Å^{-1} has been observed. The simulated neutron diffraction also shows a shoulder around this value, if the correct experimental density is

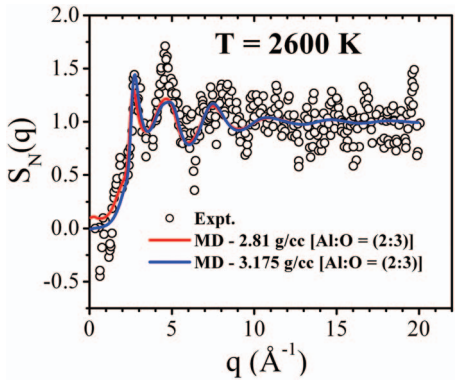

FIG. 13. (Color) Neutron static structure factor for liquid alumina at 2.81 and 3.175 g/cc and 2600 K from molecular dynamics and experiment (Refs. 13 and 14).

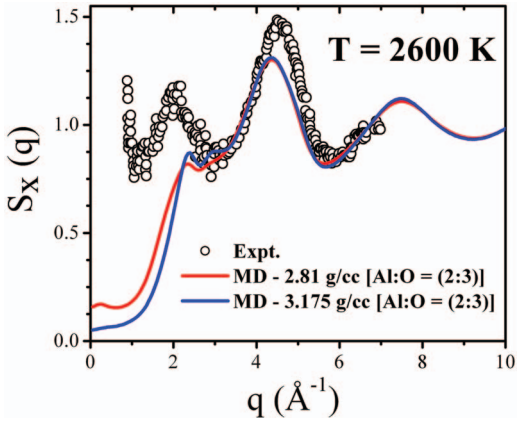

FIG. 14. (Color) X-ray static structure factor for liquid alumina at 2600 K calculated at 2.81 and 3.175 g/cc, compared to the experimental data (Ref. 11).

used. A previous simulation[47] has shown that this first sharp diffraction peak is strongly size dependent, and a higher peak is expected for large systems. In x-ray diffraction data, the most prominent peak occurs at 2.05 $Å^{-1}$.

The origin of these correlations can be inferred from the partial static structure factors in Fig. 11. The shoulder at around 1.81 $Å^{-1}$ is due to Al–O correlations, whereas the main peak at 2.7 $Å^{-1}$ arises from all correlations. The third peak in $S_N(q)$ at 4.60 $Å^{-1}$ is an average value of the Al–Al (peaked at 5.07 $Å^{-1}$), Al–O (4.10 $Å^{-1}$), and O–O (4.37 $Å^{-1}$) correlations.

The charge-charge correlation function is shown in Fig. 17 together with the neutron structure factor. Charge-charge correlations are out of phase with density-density correlations and its correlation extends beyond 10 $Å^{-1}$.

It is worth mentioning that the peaks in x-ray diffraction experiments are at 2.05 and 4.50 $Å^{-1}$, whereas they are at 1.81, 2.72, 4.6, and 7.5 $Å^{-1}$ in neutron scattering. The difference can be attributed to the different scattering mechanisms. In one case, it depends on a constant (i.e., coherent q-independent neutron cross section), and in the other case on the x-ray form factors due to scattering from electrons, which are q dependent.

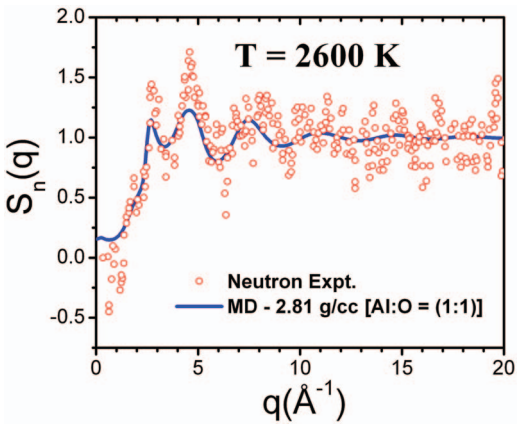

FIG. 15. (Color) Total neutron structure factor for molten alumina at 2.81 g/cc and T=2600 K from MD simulations. Here, the Al and O concentrations are taken to be $c_{Al}=c_O=0.5$ to represent oxygen deficiency [Al:O=(1:1)].

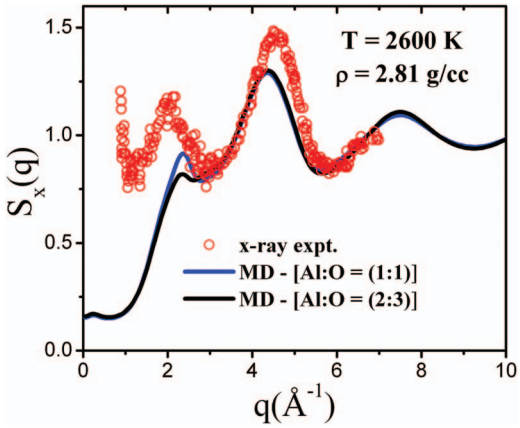

FIG. 16. (Color) X-ray structure factors for molten alumina at 2.81 g/cc and T=2600 K calculated from MD data, along with experimental results. MD calculations are displayed for stoichiometric Al:O=(2:3) and Al:O =(1:1) compositions to show the effect of oxygen deficiency.

D. Ring analysis of amorphous and liquid Al_2O_3

The connectivity of the Al_2O_3 units has been analyzed through the shortest-path ring statistics. The ring statistics is a powerful tool to understand the topology of computer-generated amorphous and glassy materials.[58–60] The shortest-path ring is defined as the shortest closed path of alternating Al–O atomic bonds. A ring size n means that n Al atoms are alternatively connected to n O atoms. For tetrahedrally coordinated systems, there are six possible paths for each atom, while in the case of octahedrally coordinated system, the number of possible paths increases to 15. We search for rings up to size of 10. Corundum (α-Al_2O_3) has only six twofold and 21 threefold rings, all of them sharing more than one octahedral edges. On the other hand, in amorphous alumina, most rings are of four- or fivefold, and very few two-, six-, and sevenfold rings exist. Table V summarizes the ring statistics per aluminum atom for corundum crystalline phase and for amorphous alumina at different densities. The absence of a larger ring size implies that the amorphous alumina does not have a large porosity.

VI. DYNAMICAL CORRELATIONS IN CRYSTALLINE, AMORPHOUS, AND MOLTEN ALUMINA

The dynamical correlations in alumina have been studied through the velocity autocorrelation function, current-current correlation function, and their Fourier transforms.

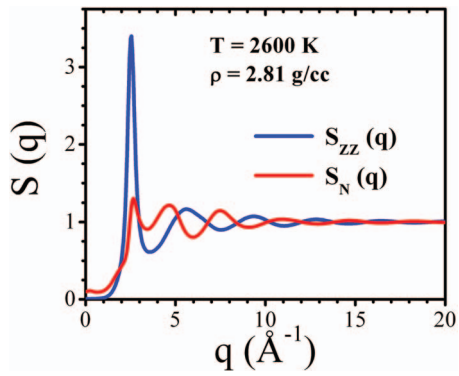

FIG. 17. (Color) Calculated charge-charge and neutron structure factors for liquid alumina at 2600 K at 2.81 g/cc.

TABLE V. Statistics of n-fold rings per number of aluminum atom in Al_2O_3 for corundum and glass phase at 2.81 g/cc.

		Ring size						
		2	3	4	5	6	7	8
Only corner sharing	Crystal	0	0	0	0	0	0	0
	Glass	0	1.764	1.725	1.155	0.159	0.032	0
One edge sharing	Crystal	0	0					
	Glass	0.313	1.286	1.841	0.806	0.103	0.004	0
More than one edge sharing	Crystal	6	21	0	0	0	0	0
	Glass	0.633	1.529	2.072	0.574	0.023	0	0
Total	Crystal	6	21	0	0	0	0	
	Glass	0.946	4.579	5.638	2.535	0.285	0.036	0

A. Velocity autocorrelation function

The velocity autocorrelation function is defined as

$$Z(t) = \frac{\langle \mathbf{v}_i(t) \cdot \mathbf{v}_i(0) \rangle}{\langle \mathbf{v}_i(0) \cdot \mathbf{v}_i(0) \rangle}, \tag{16}$$

where $\mathbf{v}_i(t)$ is the velocity of the ith atom at time t and the brackets denote averages over ensembles and atoms.

Figure 18 shows the velocity autocorrelation function for amorphous alumina at 2.81 and 3.175 g/cc. The density dependence is negligible for this density range. We have found that oxygen atoms are more correlated than aluminum, for which $Z(t)$ quickly decays to 0.

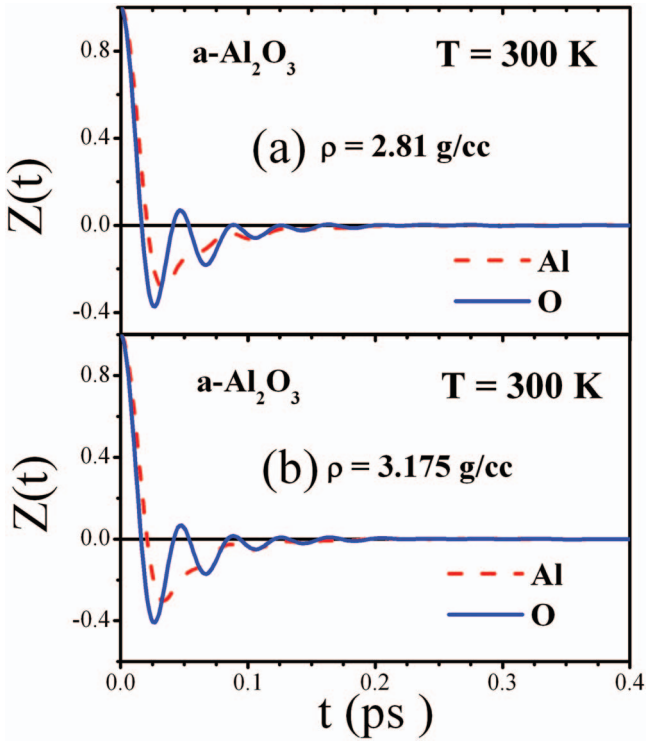

FIG. 18. (Color) Velocity autocorrelation function for amorphous alumina at 300 K and (a) 3.175 and (b) 2.81 g/cc.

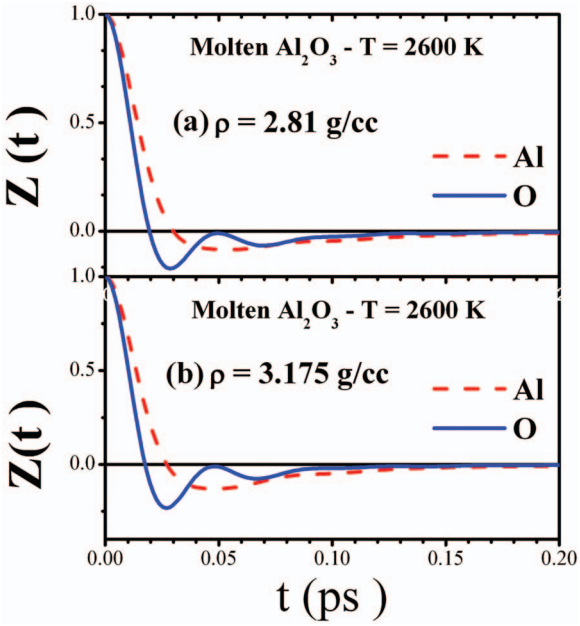

FIG. 19. (Color) Velocity autocorrelation function for molten alumina at 2600 K and (a) 2.81 and (b) 3.175 g/cc.

For molten alumina, the aluminum velocity autocorrelation function in Fig. 19 exhibits a Langevin-like autocorrelation, corresponding to a Markovian evolution (for a discussion of this kind of behavior, see the paper of Kubo on "The fluctuation-dissipation theorem"[61]). For aluminum, the velocity autocorrelation function has a decay similar to the exponential decay and it has practically no back scattering of particles in a cage of nearest neighbors. This kind of behavior will display, in the frequency spectra, a low frequency diffusive mode (see Fig. 22 below).

B. Vibrational density of states

The vibrational density of states (VDS) is determined through the Fourier transform of the corresponding velocity autocorrelation function, i.e.,

$$G_\alpha(\omega) = \frac{6N_\alpha}{\pi} \int_0^\infty Z_\alpha(t) \cos(\omega t) dt. \tag{17}$$

Figure 20 shows the calculated VDS for α-Al_2O_3 at 300 K,

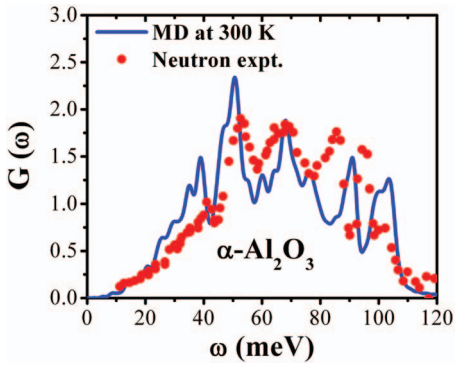

FIG. 20. (Color) Vibrational density of states calculated from velocity autocorrelation function and data from neutron scattering experiments for alpha alumina at 300 K.

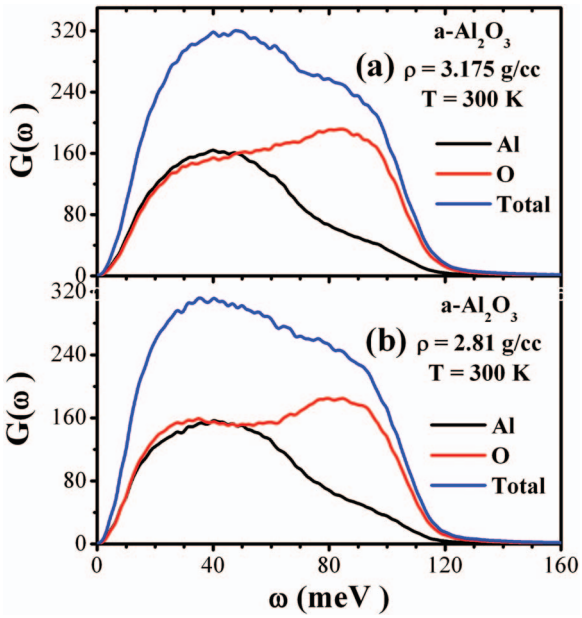

FIG. 21. (Color) Partial and total vibrational densities of states for amorphous alumina at 300 K and (a) 3.175 and (b) 2.81 g/cc.

which compares well with a neutron scattering data.[62]

Figures 21 and 22 show the partial and total VDSs for amorphous and molten alumina. The finite nonzero value of the VDS at $\omega=0$ in molten phase reflects the diffusion of the ions in this phase, $D_\alpha=(\pi k_B T/6N_\alpha m_\alpha)G(0)$, where D_α is the self-diffusion constant of species α.

The specific heat has been calculated from the vibrational density of states as a function of temperature for α-alumina and amorphous phase. Figure 23 shows the calculated specific heats for crystalline and amorphous phases at

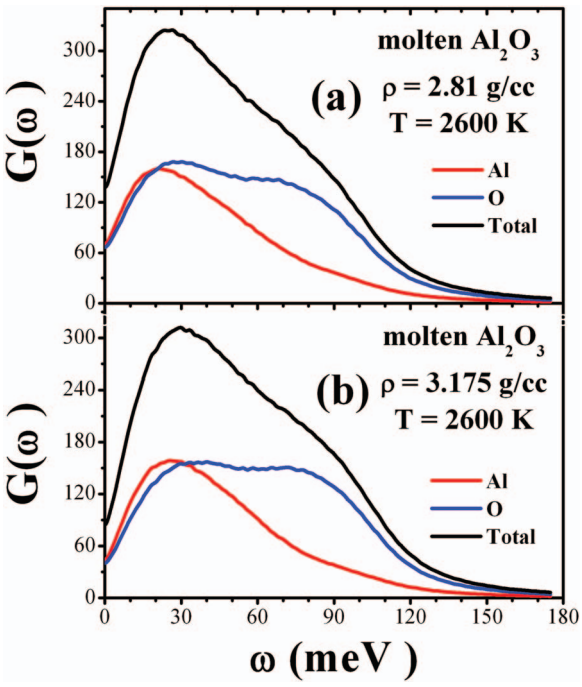

FIG. 22. (Color) Partial and total vibrational densities of states derived by Fourier transformation of the velocity autocorrelation functions for molten alumina at 2600 K and (a) 2.81 and (b) 3.175 g/cc.

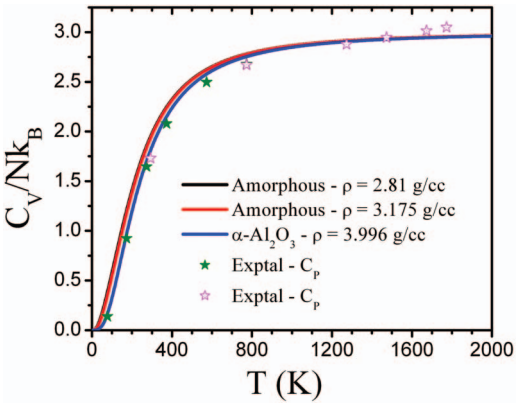

FIG. 23. (Color) Specific heats for alpha and amorphous alumina at two densities. Stars represent experimental heat capacity at constant pressure C_p for alumina (Refs. 49 and 60).

two densities. For comparison, the experimental data for C_P for selected temperatures are displayed in Fig. 23.[52,63]

C. Current-current correlation and conductivity

The current-current correlation function is defined as

$$\psi(t)=\frac{\langle \mathbf{J}(t)\cdot\mathbf{J}(0)\rangle}{\langle \mathbf{J}(0)\cdot\mathbf{J}(0)\rangle}, \tag{18}$$

where the charge current is given by

$$\mathbf{J}(t)=\sum_i Z_i e\mathbf{v}_i(t). \tag{19}$$

Figures 24 and 25 show the current-current correlation functions for amorphous and molten alumina at two densities. As expected, the molten phase hardly shows any structure beyond the first minimum.

The frequency-dependent ionic conductivity can be calculated from the Fourier transform of the current-current correlation function, i.e.,

$$\sigma(\omega)=\frac{\langle J(0)^2\rangle}{3Vk_BT}\int_0^\infty \psi(t)e^{i\omega t}dt, \tag{20}$$

where V is the volume of the system and k_B is the Boltzmann constant.

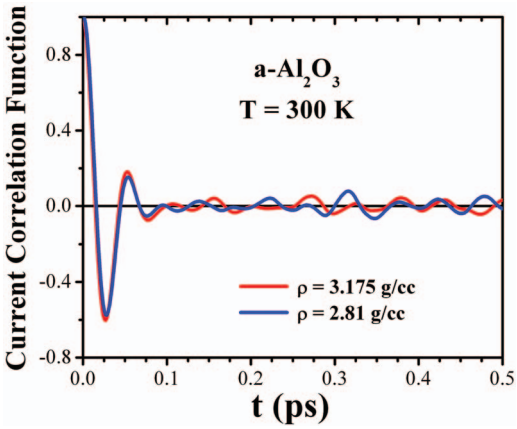

FIG. 24. (Color) Normalized current-current correlation function for amorphous alumina at two densities and 300 K.

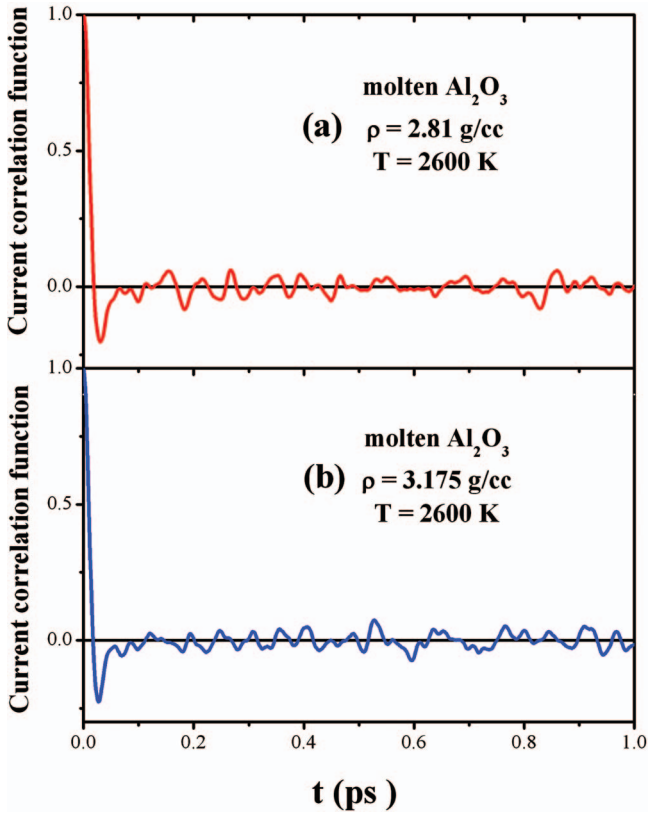

FIG. 25. (Color) Normalized current-current correlation function for molten alumina at two densities and 2600 K.

Figure 26 shows the normalized frequency-dependent conductivity for α-alumina together with frequencies from infrared experiments (shown in vertical bars in the upper part of the figure). The IR frequencies are four E_u and two A_{2u} transversal modes.[64] Since the proposed model uses screened Coulomb interaction, the LO-TO splitting cannot be described.

The corresponding normalized frequency-dependent ionic conductivities for amorphous and liquid alumina are depicted in Figs 27 and 28. The amorphous phase (Fig. 27) displays just one peak at around 70 meV and no other excitation above 120 meV. The molten alumina (Fig. 28) shows a broad spectra due to thermal effects, with the main peak

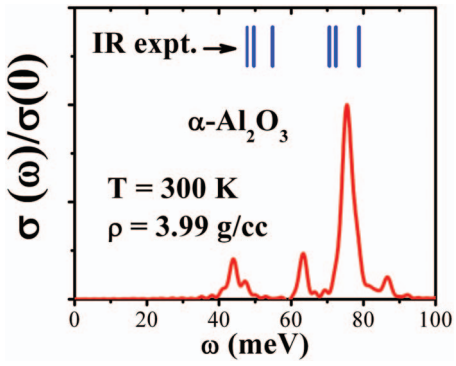

FIG. 26. (Color) Fourier transform of the normalized ionic current-current correlation function. The vertical bars are frequencies from infrared experiments for four E_u and two A_{2u} transversal symmetry modes.

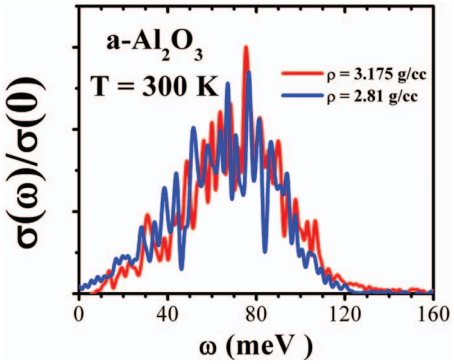

FIG. 27. (Color) Fourier transform of the normalized ionic current-current correlation for amorphous alumina at two densities and 300 K.

shifted to 60 meV and a nonzero value at $\omega=0$ (displaying the diffusive nature of the high temperature state).

VII. CONCLUSIONS

MD simulations were performed with an interatomic interaction potential developed for alumina. The proposed effective potential incorporates two- and three-body interactions. The cohesive energy, elastic constants, bulk modulus, and melting temperature of the corundum phase are well described. MD simulations with the proposed interatomic potential for the liquid state, at experimental density, characterized through neutron and x-ray structure factors are also in good agreement with the experimental results. Amorphous phases with different densities have been prepared starting from the liquid state, and the structures of amorphous and liquid states have been determined and analyzed. The statistics of shortest-path rings has been calculated for the α-crystalline and amorphous Al_2O_3. In the crystal, there are only two- and threefold rings, none of them sharing a corner of the octahedra, whereas in amorphous alumina, most of the rings are three-, four-, and fivefold. No ring size larger than 8 is found in the amorphous state. A large percentage of the rings has only corner sharing atoms: 38.5% of threefold rings, 30.6% of the fourfold rings, and 45.6% of the fivefold ring are corner sharing alone.

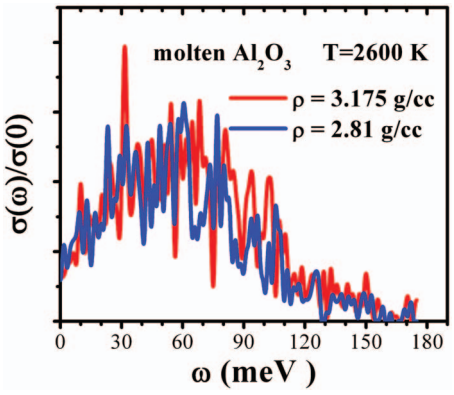

FIG. 28. (Color) Fourier transform of the normalized ionic current-current correlation function for molten alumina at two densities and 2600 K.

ACKNOWLEDGMENTS

This research was supported by ARO-MURI, DOE-BES and DOE-SciDAC, DTRA, and NSF-ITR. MD simulations were performed at the University of Southern California using the 5,384-processor Linux cluster at the Research Computing Facility and the 2,048-processor Linux cluster at the Collaboratory for Advanced Computing and Simulations. J.P.R. gratefully acknowledges financial support from Brazilian agencies Fundação de Amparo à Pesquisa do Estado de São Paulo (FAPESP) and Conselho Nacional de Desenvolvimento Científico e Tecnológico (CNPq).

[1]E. Dèorre and H. Hèubner, *Alumina: Processing, Properties, and Applications* (Springer-Verlag, Berlin, 1984).
[2]B. B. Karki, L. Stixrude, and R. M. Wentzcovitch, Rev. Geophys. **39**, 507 (2001).
[3]R. M. Wentzcovitch, C. da Silva, J. R. Chelikowsky, and N. Binggeli, Phys. Rev. Lett. **80**, 2149 (1998).
[4]I. Levin and D. Brandon, J. Am. Ceram. Soc. **81**, 1995 (1998).
[5]V. Wilms and H. Herman, Thin Solid Films **39**, 251 (1976).
[6]A. L. Dragoo and J. J. Diamond, J. Am. Ceram. Soc. **50**, 568 (1967).
[7]B. Goranchev, V. Orlinov, F. Przyborowski, and C. Weissmantel, Thin Solid Films **70**, 111 (1980).
[8]D. M. Roy, R. Roy, and T. P. O'Holleran, Bureau of Mines Final Report No. OFR 66- 81, 1980.
[9]C. G. Levi, V. Jayaram, J. J. Valencia, and R. Mehrabian, J. Mater. Res. **3**, 969 (1988).
[10]P. Lamparter and R. Kniep, Physica B **234**, 405 (1997).
[11]S. Ansell, S. Krishnan, J. K. R. Weber, J. R. Felten, P. C. Nordine, M. A. Beno, D. L. Price, and M.-L. Saboungi, Phys. Rev. Lett. **78**, 464 (1997).
[12]Y. Waseda, K. Sugiyama, and J. M. Toguri, Z. Naturforsch., A: Phys. Sci. **50**, 770 (1995).
[13]C. Landron, L. Hennet, T. E. Jenkins, G. N. Creaves, J. P. Coutures, and A. K. Soper, Phys. Rev. Lett. **86**, 4839 (2001).
[14]C. Landron, A. K. Soper, T. E. Jenkins, G. N. Greaves, L. Hennet, and J. P. Coutures, J. Non-Cryst. Solids **293**, 453 (2001).
[15]P. Florian, D. Massiot, B. Poe, I. Farnan, and J. P. Coutures, Solid State Nucl. Magn. Reson. **5**, 233 (1995).
[16]J. P. Coutures, D. Massiot, C. Bessada, P. Echegut, J. C. Rifflet, and F. Taulelle, C. R. Acad. Sci., Ser. II: Mec., Phys., Chim., Sci. Terre Univers **310**, 1041 (1990).
[17]S. Krishnan, L. Hennet, S. Jahn, T. A. Key, P. A. Madden, M. L. Saboungi, and D. L. Price, Chem. Mater. **17**, 2662 (2005).
[18]J. Guo, D. E. Ellis, and D. J. Lam, Phys. Rev. B **45**, 3204 (1992).
[19]J. Guo, D. E. Ellis, and D. J. Lam, Phys. Rev. B **45**, 13647 (1992).
[20]J. C. Boettger, Phys. Rev. B **55**, 750 (1997).
[21]B. Holm, R. Ahuja, Y. Yourdshahyan, B. Johansson, and B. I. Lundqvist, Phys. Rev. B **59**, 12777 (1999).
[22]Y. Yourdshahyan, U. Engberg, L. Bengtsson, B. I. Lundqvist, and B. Hammer, Phys. Rev. B **55**, 8721 (1997).
[23]Y. Yourdshahyan, C. Ruberto, L. Bengtsson, and B. I. Lundqvist, Phys. Rev. B **56**, 8553 (1997).
[24]T. S. Bush, J. D. Gale, C. R. A. Catlow, and P. D. Battle, J. Mater. Chem. **4**, 831 (1994).
[25]C. R. A. Catlow, R. James, W. C. Mackrodt, and R. F. Stewart, Phys. Rev. B **25**, 1006 (1982).
[26]L. Minervini, M. O. Zacate, and R. W. Grimes, Solid State Ionics **116**, 339 (1999).
[27]W. C. Mackrodt and R. F. Stewart, J. Phys. C **12**, 431 (1979).
[28]G. Paglia, A. L. Rohl, C. E. Buckley, and J. D. Galé, J. Mater. Chem. **11**, 3310 (2001).
[29]I. Manassidis, A. Devita, and M. J. Gillan, Surf. Sci. **285**, L517 (1993).
[30]G. Gutierrez, A. Taga, and B. Johansson, Phys. Rev. B **65**, 012101 (2002).
[31]E. Menendez-Proupin and G. Gutierrez, Phys. Rev. B **72**, 079904 (2005).
[32]L. J. Alvarez, J. F. Sanz, M. J. Capitan, and J. A. Odriozola, Chem. Phys. Lett. **192**, 463 (1992).
[33]L. J. Alvarez, L. E. Leon, J. F. Sanz, M. J. Capitan, and J. A. Odriozola, J. Phys. Chem. **99**, 17872 (1995).
[34]S. Blonski and S. H. Garofalini, Surf. Sci. **295**, 263 (1993).
[35]G. Paglia, A. L. Rohl, C. E. Buckley, and J. D. Gale, Phys. Rev. B **71**, 224115 (2005).
[36]G. Gutierrez, A. B. Belonoshko, R. Ahuja, and B. Johansson, Phys. Rev. E **61**, 2723 (2000).
[37]S. Jahn, P. A. Madden, and M. Wilson, Phys. Rev. B **74**, 024112 (2006).
[38]M. Matsui, Miner. Mag. **58A**, 571 (1994).
[39]R. Ahuja, A. B. Belonoshko, and B. Johansson, Phys. Rev. E **57**, 1673 (1998).
[40]M. A. S. Miguel, J. F. Sanz, L. J. Álvarez, and J. A. Odriozola, Phys. Rev. B **58**, 2369 (1998).
[41]P. Vashishta and A. Rahman, Phys. Rev. Lett. **40**, 1337 (1978).
[42]P. Vashishta, R. K. Kalia, J. P. Rino, and I. Ebbsjo, Phys. Rev. B **41**, 12197 (1990).
[43]P. S. Branicio, R. K. Kalia, A. Nakano, J. P. Rino, F. Shimogo, and P. Vashishta, Appl. Phys. Lett. **82**, 1057 (2003).
[44]P. S. Branicio, J. P. Rino, F. Shimojo, R. K. Kalia, A. Nakano, and P. Vashishta, J. Appl. Phys. **94**, 3840 (2003).
[45]P. Vashishta, R. K. Kalia, A. Nakano, and J. Rino, J. Appl. Phys. **101**, 103515 (2007).
[46]M. P. Allen and D. J. Tildesley, *Computer Simulation of Liquids* (Clarendon, Oxford, 1987).
[47]A. Nakano, R. K. Kalia, and P. Vashishta, J. Non-Cryst. Solids **171**, 157 (1994).
[48]P. Vashishta, R. K. Kalia, A. Nakano, and J. P. Rino, Phys. Rev. B (to be published).
[49]J. H. Gieske and G. R. Barsch, Phys. Status Solidi **29**, 121 (1968).
[50]F. D. Murnaghan, Proc. Natl. Acad. Sci. U.S.A. **30**, 244 (1944).
[51]P. Tyrolero and W. K. Lu, J. Am. Ceram. Soc. **52**, 77 (1969).
[52]NIST Structural Ceramics Database (SCD) (http://www.ceramics.nist.gov).
[53]N. Ishizawa, T. Miyata, I. Minato, F. Marumo, and S. Iwai, Acta Crystallogr., Sect. B: Struct. Crystallogr. Cryst. Chem. **36**, 228 (1980).
[54]R. S. Zhou and R. L. Snyder, Acta Crystallogr., Sect. B: Struct. Sci. **47**, 617 (1991).
[55]G. Gutierrez and B. Johansson, Phys. Rev. B **65**, 012101 (2002).
[56]B. Glorieux, F. Millot, J. C. Rifflet, and J. P. Coutures, Int. J. Thermophys. **20**, 1085 (1999).
[57]M. Hemmati, M. Wilson, and P. A. Madden, J. Phys. Chem. B **103**, 4023 (1999).
[58]J. P. Rino, I. Ebbsjo, R. K. Kalia, A. Nakano, and P. Vashishta, Phys. Rev. B **47**, 3053 (1993).
[59]I. Ebbsjo, R. K. Kalia, A. Nakano, J. P. Rino, and P. Vashishta, J. Appl. Phys. **87**, 7708 (2000).
[60]H. Iyetomi, P. Vashishta, and R. K. Kalia, J. Non-Cryst. Solids **262**, 135 (2000).
[61]R. Kubo, Rep. Prog. Phys. **29**, 255 (1966).
[62]C.-K. Loong, J. Eur. Ceram. Soc. **19**, 2241 (1999).
[63]National Physics Laboratory (www.kayelaby.npl.co.uk/general_physics/).
[64]A. S. Barker, Phys. Rev. **132**, 1474 (1963).